Chapter 5

An analytical viscous model for steady-state atmospheric vortices

5.1 Introduction

In the existing models of atmospheric vortices, there are often idealisations such as neither radial nor axial components of velocity (Lamb (1932), Oseen (1911), Pandey and Maurya (2018b), Rankine (1882), Taylor (1918)) or radial velocity depending only on the radial coordinate (Long (1961), Rott (1958)), or a special form of viscosity Kieu and Zhang (2009)) and so on. Steady-state models (Lamb (1932), Oseen (1911), Rankine (1882), Taylor (1918), Long (1961), Rott (1958), Kieu and Zhang (2009), Burgers (1948)) are often used for validation of observed experimental data and numerical simulation. Azimuthal velocity in such models attains the maximum at a radius called the characteristic

The contents of this chapter are published in **Physica Scripta, IOP Science**, (7), **99**(2024)075233.

radius and then starts to diminish in the outer region of the vortex and approaches zero as $r \to \infty$. Such models lead to an ideal formulation that fits to special circumstances only. However, some other researchers Makarieva et al. (2011) and Pandey and Maurya (2017) built more general models. Those models were based on more generic versions of velocity components while still modelling a unique situation that the radial velocity vanishes at a particular height. In fact, the radial velocity of an atmospheric vortex has a particular form created by the circumstances surrounding the vortex where it forms.

The Rankine (1882) and Burgers (1948) models are frequently used to study and analyse single-celled atmospheric vortices, while the Sullivan (1959) is used to model double-celled vortices. Sullivan (1959) gave an exact solution with some analogy to the Burgers (1948); Rott (1958). He worked on both one-celled and two-celled vortices and proposed a model for steady viscous incompressible flow. The steady two-celled viscous vortex solution of Sullivan (1959) was extended to obtain unsteady two-celled viscous vortex solutions which act asymptotically similar to unsteady one-celled solutions of Rott (1958). The Sullivan model put forward the flow of an intense atmospheric vortex having a central downdraft. The atmospheric vortices existing in nature die out after some time. Therefore the velocity components are bounded. However, some models exhibit an unbounded velocities (Gillmeier et al. (2018), Kim and Matsui (2017), Wood and Brown (2011)) and hence carry this drawback forward.

Kuo (1971) formulated a 3-D flow in the boundary layer of tornadoes with vorticity within the core region and zero vorticity in the peripheral zone, and solved nonlinear equations for vertical and radial velocity components. Ward (1972) simulated in a laboratory, the three features of tornadoes, viz., characteristic surface pressure profile, bulging deformation on the vortex core, and multiple vortices in a single convergence system. Church and Snow (1979) interpreted numerically the dynamics of a tornado-like vortex using the Large Eddy Simulation (LES) turbulence model. Vatistas et al. (1991)

used experimental observations to determine the vortex's hydrodynamic characteristics. They used a new formulation of the Navier-Stokes equation to get the azimuthal velocity distribution. In the axial direction, the tangential velocity component hardly varies. The azimuthal momentum equation can therefore be used to compute radial velocity component under certain assumptions. Vatistas et al. (1991) presented tangential velocity profiles for vortices with continuous flow distributions. Haan Jr et al. (2008) designed a laboratory tornado to generate tornado-like vortices for aerodynamic loads on civil engineering structures. Refan et al. (2014) experimentally simulated atmospheric vortices which are related to tornadoes in order to demonstrate proper kinematic and dynamic scaling. To understand the real mechanism adhering to the atmospheric vortex flow field, a simple mathematical model is required, which reduces the existence of error in the observed data and allows explaining real velocities and pressure fields. Doppler radars are being used by researchers to enable full-scale tornado data from a secure distance. However, the information gathered from such measures is primarily restricted to the tornado genesis (Bluestein (2005), Bluestein et al. (1993), Bluestein et al. (2003), Davies-Jones and Wood (2006), Lewellen et al. (1997), Wurman et al. (1996)). Lewellen et al. (1997) used LES to analyse the influence of translation and surface roughness on tornado-like vortices.

According to Vyas and Majdalani (2006), an inviscid solution describes the cyclonic motion of an axi-symmetrical vortex in a cylindrical chamber for an incompressible, steady fluid. The duo Vyas et al. (2003) further gave a solution for the viscous core of the bidirectional flow field using the Navier-stokes equations in cylindrical polar coordinates arising in a swirl-driven thrust chamber. Xu and Hangan (2009) formulated an inviscid flow vortex model for tornadoes using free narrow jet solution with the modified Rankine (1882) model. The combined model is not an exact solution of Navier-Stokes equations. Kieu and Zhang (2009) presented an analytical model of tropical cyclones to investigate rapid intensification from the perspective of rotational growth under the consideration that

the viscosity of the fluid follows a particular form. They attributed the presence of a double exponential form as the reason for intensification. Pandey and Maurya (2020) endorsed the reason, however, even for general viscosity.

Wood and White (2011) designed a new parametric model of vortex tangential wind profiles based on the model of Vatistas et al. (1991). It was constructed for a more realistic tangential wind profile observed in atmospheric vortices such as tornadoes, and dust devils. Natarajan and Hangan (2012) modelled tornado large eddy simulations of translation and surfaces roughness was simulated by adding a momentum term in the momentum equation; Liu and Ishihara (2016) investigated the roughness and translation of air vortices resembling tornadoes. Gillmeier et al. (2016) analysed the influence of a tornado generator's geometry on the flow field; Gillmeier et al. (2016) worked on the relationships between convective forcing and tornado intensity, and their impact on tornado structure. Ying and Chang (1970) opine, "Tornado is a huge vortex column with a low-pressure visual core," and with this consideration, Pandey and Maurya (2017) presented a generic model exploring the fundamental characteristics of whirlwinds. However, they examined dust devils in detail. Baker and Sterling (2017) presented an article for inviscid vortex flows in which velocity components $\bar{u} = \frac{k\delta\bar{r}\bar{z}}{(1+\bar{r}^2)(1+\bar{z}^2)}$ where δ is the ratio between the vertical and horizontal length scales $\bar{v} = \frac{k\bar{r}ln(1+\bar{z}^2)}{(1+\bar{r}^2)}$ (k being arbitrary constant) and $\bar{w} = \frac{4\delta ln(1+\bar{z}^2)}{(1+\bar{r}^2)^2}$ from the Euler equation. The viscous effects remained untouched. This model analysed the trajectories of wind-borne debris in tornado wind fields. Pandey and Maurya (2018a) presented an exact solution for the unsteady flow of atmospheric vortices, an extension of Burgers (1948) model. Some recent articles (Davies-Jones and Wood (2006), Onishchenko et al. (2021b), Onishchenko et al. (2019), Onishchenko et al. (2018), Onishchenko et al. (2014b)) reported some mathematical models and presented analytical solutions for atmospheric vortices. Onishchenko et al. (2021b) presented a novel analytical solution of equations governing quasi-stationary vortices in the Earth's atmosphere

of an inviscid fluid. There are a few more analytical models describing various features available in the literature (Davies-Jones et al. (2001), Horton et al. (2016), Kolomenskiy and Moffatt (2012), Moffatt (2000), Onishchenko et al. (2014b), Rotunno (2013)).

Onishchenko et al. (2021b) presented analytical solutions of equations governing steady concentrated vortices of inviscid and incompressible fluid. Authors obtained analytical solutions by assuming stream function and obtaining radial component of velocity of the form $u(r,z) = v_0 \frac{r}{r_0}(1 - \frac{z}{L})exp(-\frac{z}{L} - \frac{r^2}{r_0^2})$, where r, z are respectively radial coordinate, the axial coordinate, and v_0, L, r_0 represent the characteristic azimuthal velocity, the characteristic length and the characteristics radius at which maximum azimuthal velocity occurs. They made an additional assumption that this radial velocity profile would meet the boundary condition $u(r,z) = 0$ for $r = 0$ and $\frac{r}{r_0} >> 1$ and $\frac{z}{L} >> 1$. They thus obtained pressure, azimuthal velocity and vertical velocity for steady axi-symmetric flow of an incompressible inviscid fluid. This radial profile of velocity is exponentially localized in both radial and vertical directions; and flow parameters are characterized not only by a characteristic vortex radius but also by a characteristic vortex height. It was concluded by Makarieva et al. (2011) "The decrease of pressure along the vertical axis sustains the ascending air motion with vertical velocity w and induces a compensating horizontal air inflow with radial velocity $u(r,z)$. The converging radial flow has a maximal velocity at the surface where the magnitude of the condensation-induced pressure drop is the largest. Radial velocity approaches zero at a certain height $z = h$, which approximately coincides with the cloud height."

In literature, a number of research papers are available on experimental/laboratory models whose results have been simulated against theoretical models (Gillmeier et al. (2017) ; Horn and Aurnou (2021); Refan et al. (2017)). Tang et al. (2018) devised a tornado-like simulator and compared their experimental results with theoretical

vortices formulated by Rankine (1882) and Burgers (1948) for various swirl ratios and radial Reynolds number.

In this article, we, however, intend to explore new analytical solutions for viscous and incompressible axi-symmetric flows of atmospheric vortices with a more generic form of velocity components. We assume the radial component $u(r, z)$ of velocity as a function of r and z both, which is in agreement with the conclusion of Makarieva et al. (2011). Motion is being considered steady. However, we intend to give due importance on viscosity despite the fact that atmospheric vortices have very large Reynolds number in the range $1000 - 10000$. On account of very large Reynolds number the viscosity effects are expected to be very small, but inviscid considerations are an idealisation of true models to avoid complexity involved in obtaining solutions. In reality, no fluid is inviscid. The assumptions made are expected to modify azimuthal and vertical velocities, and pressure distribution to a large extent.

5.2 Mathematical formulation of the problem

We consider a three-dimensional steady axi-symmetric atmospheric vortex in cylindrical polar coordinates $(\tilde{r}, \tilde{\theta}, \tilde{z})$ where $\tilde{r}$, $\tilde{\theta}$ and $\tilde{z}$ are respectively radial, azimuthal and axial coordinates, because it is believed to be formed as a rotational motion around some vertical axis. Let radial velocity depend on both radial and vertical coordinates. Thus, the system of equations governing the steady axi-symmetric motion of incompressible viscous fluids is given by

$$\left(\tilde{u}\frac{\partial \tilde{u}}{\partial \tilde{r}} + \tilde{w}\frac{\partial \tilde{u}}{\partial \tilde{z}} - \frac{\tilde{v}^2}{\tilde{r}}\right) = -\frac{1}{\rho}\frac{\partial \tilde{p}}{\partial \tilde{r}} + \nu\left(\frac{\partial^2 \tilde{u}}{\partial \tilde{r}^2} + \frac{1}{\tilde{r}}\frac{\partial \tilde{u}}{\partial \tilde{r}} - \frac{\tilde{u}}{\tilde{r}^2} + \frac{\partial^2 \tilde{u}}{\partial \tilde{z}^2}\right), \tag{5.1}$$

$$\left(\tilde{u}\frac{\partial \tilde{v}}{\partial \tilde{r}} + \tilde{w}\frac{\partial \tilde{v}}{\partial \tilde{z}} + \frac{\tilde{u}\tilde{v}}{\tilde{r}}\right) = \nu\left(\frac{\partial^2 \tilde{v}}{\partial \tilde{r}^2} + \frac{1}{\tilde{r}}\frac{\partial \tilde{v}}{\partial \tilde{r}} - \frac{\tilde{v}}{\tilde{r}^2} + \frac{\partial^2 \tilde{v}}{\partial \tilde{z}^2}\right), \tag{5.2}$$

$$\left(\tilde{u}\frac{\partial\tilde{w}}{\partial\tilde{r}}+\tilde{w}\frac{\partial\tilde{w}}{\partial\tilde{z}}\right)=-\frac{1}{\rho}\frac{\partial\tilde{p}}{\partial\tilde{z}}+\tilde{F}_z+\nu\left(\frac{\partial^2\tilde{w}}{\partial\tilde{r}^2}+\frac{1}{\tilde{r}}\frac{\partial\tilde{w}}{\partial\tilde{r}}+\frac{\partial^2\tilde{w}}{\partial\tilde{z}^2}\right), \tag{5.3}$$

together with the continuity equation

$$\frac{1}{\tilde{r}}\frac{\partial(\tilde{r}\tilde{u})}{\partial\tilde{r}}+\frac{\partial\tilde{w}}{\partial\tilde{z}}=0, \tag{5.4}$$

where $\tilde{u}$, $\tilde{v}$, $\tilde{w}$ and ν respectively stand for the radial, azimuthal, axial components of velocity, and the kinematic viscosity of the fluid. $\tilde{p}$ is pressure, $\tilde{F}_z = g(\rho-\rho_\infty)/\rho_\infty$ buoyancy, g the gravitational acceleration and ρ, ρ_∞ respectively the densities of the vortex and the ambient wind.

5.2.1 Non-dimensionalization

For the sake of dynamical similarity, we non-dimensionalize the governing equations (5.1-5.4) by means of the following dimensionless variables

$$r=\frac{\tilde{r}}{r_m}, z=\frac{\tilde{z}}{L}, v=\frac{\tilde{v}}{v_m}, w=\frac{\tilde{w}}{v_m}, p=\frac{\tilde{p}}{\rho v_m^2}, F=\frac{\tilde{F}_z}{v_m^2/r_m}, \tag{5.5}$$

v_m being the maximum azimuthal velocity at the core radius r_m and L the characteristic height of the atmospheric vortex. In view of (5.5), Eqs. (5.1-5.4) are transformed to

$$u\frac{\partial u}{\partial r}+\alpha w\frac{\partial u}{\partial z}-\frac{v^2}{r}=-\frac{\partial p}{\partial r}+\frac{1}{Re}\left(\frac{\partial^2 u}{\partial r^2}+\frac{1}{r}\frac{\partial u}{\partial r}+\alpha^2\frac{\partial^2 u}{\partial z^2}-\frac{u}{r^2}\right), \tag{5.6}$$

$$u\frac{\partial v}{\partial r}+\alpha w\frac{\partial v}{\partial z}+\frac{uv}{r}=\frac{1}{Re}\left(\frac{\partial^2 v}{\partial r^2}+\frac{1}{r}\frac{\partial v}{\partial r}+\alpha^2\frac{\partial^2 v}{\partial z^2}-\frac{v}{r^2}\right), \tag{5.7}$$

$$u\frac{\partial w}{\partial r}+\alpha w\frac{\partial w}{\partial z}=-\alpha\frac{\partial p}{\partial z}+F+\frac{1}{Re}\left(\frac{\partial^2 w}{\partial r^2}+\frac{1}{r}\frac{\partial w}{\partial r}+\alpha^2\frac{\partial^2 w}{\partial z^2}\right), \tag{5.8}$$

$$\frac{1}{r}\frac{\partial}{\partial r}(ru)+\alpha\frac{\partial w}{\partial z}=0, \tag{5.9}$$

where $\alpha = r_m/L$, $Re = v_m r_m/\nu$ denotes the Reynolds number and $F = \tilde{F}_z/(v_m^2/r_m)$.

5.2.2 Empirical consideration of radial wind component

This model is based on the notion that the radial component of velocity u is not only a function of r but also of z. Following Onishchenko et al. (2021b), we divide the geometry of the problem into two parts: (1) convergence zone and (2) convective zone. The convergence zone is also referred to as the boundary layer zone in which surrounding winds enter the centre of the vortex, which extends from the ground $z = 0$ to some height $z = d$. The region above d is the convective zone.

Pandey and Maurya (2018b) considered the linear vertical profile of radial velocity as $u(r, z) = -(1 - \frac{az}{h})\frac{r}{1+r^2}$, for $0 \leq z < h$, where the parameter a controls the shape of the function $u_2(z)$ and $u_2(z) = 0$ for $h \leq z$, i.e. radial velocity $u(r, z)$ vanishes above the height h. Onishchenko et al. (2021b) considered a bit more general form $u(r, z) = -v_0\frac{r}{r_0}(1 - \frac{z}{L})exp(-\frac{z}{L} - \frac{r^2}{r_0^2}))$, as discussed in the introduction. However, in this study, we make the assumption that the radial component of velocity $u(r, z)$ has the most realistic profile that fits the observational data. It is widely acknowledged that radial velocity decreases with height and disappears along the axis of symmetry as well as at a specific height from the ground (z-axis). We incorporate radial velocity from Onishchenko et al. (2021b) in our study. The radial and axial coordinates of radial velocity are normalized with the radius r_m at which the azimuthal velocity v_m is maximum. The reduced radial velocity is therefore given by

$$u(r, z) = -\alpha r(1 - z)e^{-z-r^2}, \tag{5.10}$$

where α is a non-dimensional constant. Here negative sign indicates that the winds are blowing toward the centre of the vortex. Substituting $u(r,z)$ from Eq. (5.10) into continuity equation Eq. (5.9), we obtained axial velocity as

$$w(r,z) = 2z(1-r^2)e^{-z-r^2}. \tag{5.11}$$

Substituting $u(r,z)$ from Eq. (5.10) and $w(r,z)$ from Eq. (5.11) into Eq. (5.6), we get

$$\begin{aligned}\frac{v^2}{r} - \frac{\partial P}{\partial r} &= r\alpha^2(1-2r^2+z(2-z))e^{-2(z+r^2)} \\ &\quad - \frac{\alpha}{Re}\left[4r(2-r^2)(1-z) - \alpha^2 r(3-z)\right]e^{-(z+r^2)},\end{aligned} \tag{5.12}$$

and further substituting $u(r,z)$ and $w(r,z)$ into Eq. (5.8), we get

$$-\alpha\frac{\partial P}{\partial z} + F = 4\alpha z(1-z)e^{-2(z+r^2)} - \frac{2}{Re}\left(-4(2-4r+r^4)z - \alpha^2((2-z)(1-r^2))\right)e^{-(z+r^2)}. \tag{5.13}$$

Integrating Eq. (5.13), with respect to z, we get

$$\begin{aligned}-\alpha p + zF =& 2\alpha z^2 e^{-2(z+r^2)} - \frac{2}{Re}\Big(4(2-4r+r^4)(1+z) + \alpha^2((1-z)(1 \\ &- r^2))\Big)e^{-(z+r^2)} + A(r),\end{aligned} \tag{5.14}$$

where $A(r)$ is an arbitrary function of r; and then differentiating Eq. (5.14) with respect to r, we obtain

$$\begin{aligned}-\alpha\frac{\partial p}{\partial r} =& -8r\alpha z^2 e^{-2(z+r^2)} + \frac{2}{Re}\Big(8r(6-6r^2+r^4)(1+z) + 2r\alpha^2(2-r^2)(1 \\ &- z)\Big)e^{-(z+r^2)} + \frac{dA(r)}{dr}.\end{aligned} \tag{5.15}$$

Substitution of $-\frac{\partial p}{\partial r}$ from Eq. (5.15) into Eq. (5.12) yields the azimuthal component of velocity

$$v(r,z) = \Bigg[r^2\{\alpha^2(1-2r^2+z(2-z))+8z^2\}e^{-2(z+r^2)} - \frac{1}{Re}\Bigg(8\alpha(2-r^2)(1-z) - \alpha^3(3-z) + \frac{16}{\alpha}(6-6r^2+r^4)(1+z)\Bigg)e^{-(z+r^2)} - \frac{r}{\alpha}\frac{dA(r)}{dr}\Bigg]^{1/2}, \quad (5.16)$$

where $A(r)$ will be evaluated in the subsequent section. A solution of Eq. (5.7) should give $v(r,z)$. But so far no such method has been discovered to get an exact solution of such an involved non-linear equation. However, various approximations based on low and high Reynolds numbers or series approximation are in practice. Besides, numerical approximations are also popular. Therefore, we resort to the following method to evaluate $A(r)$ which is the only unknown in $v(r,z)$ given by Eq. (5.16).

5.2.3 Evaluation of $A(r)$

To evaluate the arbitrary function $A(r)$, we use the Rankine model as a boundary condition at $z=0$. The Rankine model involves the azimuthal component of velocity v for incompressible and steady flow with no radial and vertical components. The Rankine model combines two distinct vortex flows for the two regions, called inner and outer regions, separated at an interface. The interior region of the vortex has solid body rotation flow whereas the outer region of the vortex has potential type flows. They are symbolized as

$$v(r,0) = \tilde{v}(\tilde{r},0)/v_m = r \quad for \quad r = \tilde{r}/r_m \leq 1$$
$$v(r,0) = \tilde{v}(\tilde{r},0) = 1/r \quad for \quad r = \tilde{r}/r_m \geq 1$$

Substituting $z = 0$ into Eq. (5.15), we get

$$\frac{dA(r)}{dr} = -\alpha \frac{\partial p(r,0)}{\partial r} - \frac{4r}{Re}\Big(2(6 - 6r^2 + r^4) + \alpha^2(2 - r^2)\Big)e^{-r^2}, \tag{5.17}$$

and then its integration yields

$$A(r) = -\alpha \int \frac{\partial p(r,0)}{\partial r} dr \; - \frac{2}{Re}\Big(4(-2 + 4r^2 - r^4) + \alpha^2(r^2 - 1)\Big)e^{-r^2} + C. \tag{5.18}$$

where C is an integrating constant.

5.2.3.1 Evaluation of $A(r)$ for the region $r = \tilde{r}/r_m \leq 1$.

In this subsection, we determine $A(r)$ in the inner region $r = \tilde{r}/r_m \leq 1$ of the vortex. Azimuthal velocity is subsequently derived as

$$\begin{aligned} v(r,z) = \Bigg[& r^2\{\alpha^2(1 - 2r^2 + z(2 - z)) + 8z^2\}e^{-2(z+r^2)} \\ & - \frac{1}{Re}\Big(8\alpha(2 - r^2)(1 - z) - \alpha^3(3 - z) + \frac{16}{\alpha}(6 - 6r^2 + r^4)(1 + z)\Big)e^{-(z+r^2)} \\ & + \frac{r}{\alpha}\Big(\alpha r + \frac{4r}{Re}\{2(6 - 6r^2 + r^4) - \alpha(2 - r^2)\}e^{-r^2}\Big)\Bigg]^{1/2}. \end{aligned} \tag{5.19}$$

and pressure as

$$\begin{aligned} -\alpha\{p(r,z) - p(0,0)\} = & -zb_z + 2\alpha z^2 e^{-2(z+r^2)} \\ & - \frac{2}{Re}\Big[4(1 + z)(2 - 4r^2 + r^4) + \alpha^2\{(1 - z)(1 - r^2)\}\Big]e^{-(z+r^2)} \\ & - \alpha\frac{r^2}{2} - \frac{2}{Re}\Big[4(-2 + 4r^2 - r^4) + \alpha^2(r^2 - 1)\Big]e^{-r^2}. \end{aligned} \tag{5.20}$$

The details of the calculations are presented in Appendix (A).

5.2.3.2 Evaluation of $A(r)$ for the region $r = \tilde{r}/r_m \geq 1$

Following section 5.2.3.1, we evaluate azimuthal velocity for the region $r = \tilde{r}/r_m \geq 1$ as

$$v(r,z) = \Bigg[r^2 \Big\{ \alpha^2(1 - 2r^2 + z(2-z)) + 8z^2 \Big\} e^{-2(z+r^2)} - \frac{1}{Re} \Bigg(8\alpha(2-r^2)(1-z) - \alpha^3(3-z) + \frac{16}{\alpha}(6 - 6r^2 + r^4)(1+z) \Bigg) e^{-(z+r^2)} + \frac{r}{\alpha} \left(\frac{\alpha}{r^3} + \frac{4r}{Re} \Big\{ 2(6 - 6r^2 + r^4) - \alpha^2(2-r^2) \Big\} e^{-r^2} \right) \Bigg]^{1/2}. \tag{5.21}$$

and pressure

$$-\alpha \Big\{ p(r,z) - p(1,0) \Big\} = -zF + 2\alpha z^2 e^{-2(z+r^2)} - \frac{2}{Re} \Big[4(1+z)(2 - 4r^2 + r^4) + \alpha^2(1-z)(1-r^2) \Big] e^{-(z+r^2)} + \frac{\alpha}{2} \left(\frac{1}{r^2} - 1 \right) - \frac{2}{Re} \Big[4(-2 + 4r^2 - r^4) + \alpha^2(r^2 - 1) \Big] e^{-r^2}. \tag{5.22}$$

The details of the calculations are presented in Appendix (B).

5.2.3.3 Evaluation of $A(r)$ with Burger's model

$A(r)$ may be determined from Burger's model, given in the dimensionless form, as $v(r,0) = (1 - exp(-Kr^2))/r$, K being a constant under similar conditions. It gives $\frac{\partial p(r,0)}{\partial r} = \frac{(1-e^{-Kr^2})^2}{r^3}$, using the condition that at $z = 0$ the flow satisfies the cyclostrophic balance i.e. $\partial p(r,0)/\partial r = v^2(r,0)/r$. Substituting the velocity $v(r,0)$ of Burger's model into $\partial p(r,0)/\partial r = v^2(r,0)/r$, we get

$$\frac{\partial p(r,0)}{\partial r} = \frac{(1 - e^{-Kr^2})^2}{r^3}. \tag{5.23}$$

Now from Eq. (5.17) and Eq. (5.22), we have

$$\frac{dA(r)}{dr} = -\alpha\frac{(1-e^{-Kr^2})^2}{r^3} - \frac{4r}{Re}\Big(2(6-6r^2+r^4)+\alpha^2(2-r^2)\Big)e^{-r^2} \tag{5.24}$$

which, on integration, gives

$$A(r) = -\alpha\int\frac{(1-e^{-Kr^2})^2}{r^3}dr - \frac{2}{Re}\Big(4(-2+4r^2-r^4)+\alpha^2(r^2-1)\Big)e^{-r^2}+C. \tag{5.25}$$

Hence we obtain azimuthal velocity

$$\begin{aligned} v(r,z) = \Bigg[& r^2\{\alpha^2(1-2r^2+z(2-z))+8z^2\}e^{-2(z+r^2)} - \frac{1}{Re}\Big(8\alpha(2-r^2)(1-z) \\ & -\alpha^3(3-z)+\frac{16}{\alpha}(6-6r^2+r^4)(1+z)\Big)e^{-(z+r^2)} + \frac{(1-e^{-Kr^2})^2}{r^2} \\ & + \frac{4r^2}{\alpha Re}\Big(2(6-6r^2+r^4)+\alpha(2-r^2)\Big)e^{-r^2}\Bigg]^{1/2}, \end{aligned} \tag{5.26}$$

and pressure as

$$\begin{aligned} \{p(r,z)-p(1,0)\} = \frac{-1}{\alpha}\Bigg[& -zF + 2\alpha z^2 e^{-2(z+r^2)} \\ & - \frac{2}{Re}\Big(4(1+z)(2-4r^2+r^4)+\alpha^2\{(1-z)(1-r^2)\}\Big)e^{-(z+r^2)} \\ & - \alpha\Bigg[\int\frac{(1-e^{-Kr^2})^2}{r^3}dr - \Big(\int\frac{(1-e^{-Kr^2})^2}{r^3}dr\Big)_{r=0}\Bigg] \\ & - \frac{2}{Re}\Big(4(-2+4r^2-r^4)+\alpha^2(r^2-1)\Big)e^{-r^2}\Bigg]; \end{aligned} \tag{5.27}$$

intermediate steps for the evaluation of pressure are given in Appendix (C).

5.3 Results and discussion

In this article, we tried to explore a more generalized model for atmospheric vortices for a viscous and incompressible fluid. Analytical solutions of the equations governing the atmospheric vortices whose velocity components depend on radial and vertical coordinates both, and which are further more compatible with real-life phenomena have been derived.

This model addresses several limitations observed in earlier approaches, especially when compared to the traditional Rankine (1882) vortex, Sullivan (1959) vortex and Baker and Sterling (2017) vortex models. The Rankine (1882) model simplifies the flow by neglecting radial and axial velocity components, and it represents azimuthal velocity as a combination of a forced vortex core and a free vortex outer region. It fails to describe the real-world vortex phenomena. The Burger-Rott, introduced the idea of three non-zero velocity components. However, it assumes that vertical velocity is a function of height z but lacks radial dependence, a feature that is unrealistic. Moreover, radial and vertical velocities both in the Burger-Rott model are unbounded. This behaviour has limited applicability, particularly at high altitudes and large radial distances. The Sullivan (1959) vortex, offers some improvements over the Burger-Rott model. It introduces a more complex vortex structure but again there is no bound on radial and axial velocities in the radial direction. Baker and Sterling (2017) gave a more generalized model for tornado vortex for inviscid flow with a bounded radial component but still, the azimuthal and the vertical components are unbounded.

5.3.1 Radial velocity $u(r, z)$

The radial component of velocity is based on the model of Onishchenko et al. (2021b) for inviscid, incompressible and steady flows. Fig. (5.1) displays the radial profile of the

radial velocity which is factually directed towards the centre and hence is negative in the formula. It is observed that the radial velocity increases in magnitude to the maximum at the outer boundary of the core, decreases further and vanishes as it reaches the axis.

The radial velocity, which depends also on the axis as per the supposition, is observed to reduce in magnitude with height, eventually vanishing at $z = 1$ in accordance with the formula given in Eq. (5.10). For further higher values of z, the radial velocity appears to move in the opposite direction following the formula. However, the magnitude is quiet meagre which also ultimately dies out i.e., $u \to 0$ as $z \to \infty$. Unlike Burgers and Rankine models for single-cell vortices, this model satisfies real boundary conditions on the radial velocity.

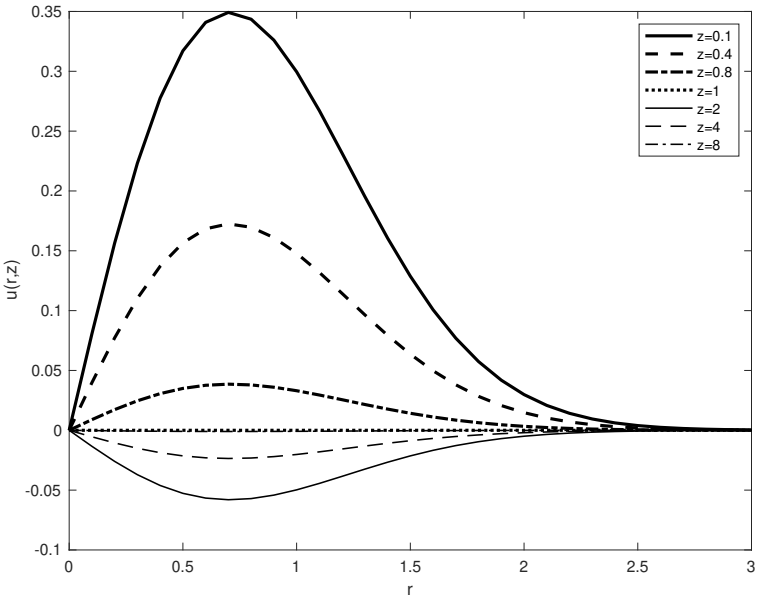

Figure 5.1: Plots of the radial profile of radial velocity for different heights

5.3.2 Vertical velocity $w(r, z)$

Figs. (5.2a-b) display the radial profiles of the computed vertical velocity $w(r, z)$ based on the formula given in Eq. (5.11) for different heights. It is observed that the vertical velocity tends to decrease as one moves away from the centre of the vortex to be zero identically at $r = 1$ in accordance with the formula given by Eq. (5.11), beyond which there is no vertical velocity.

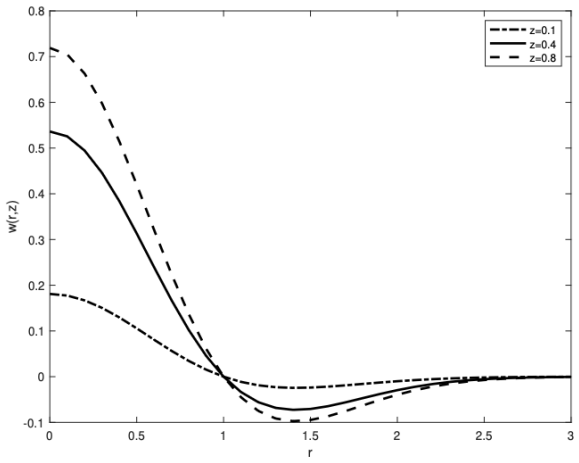

(a)

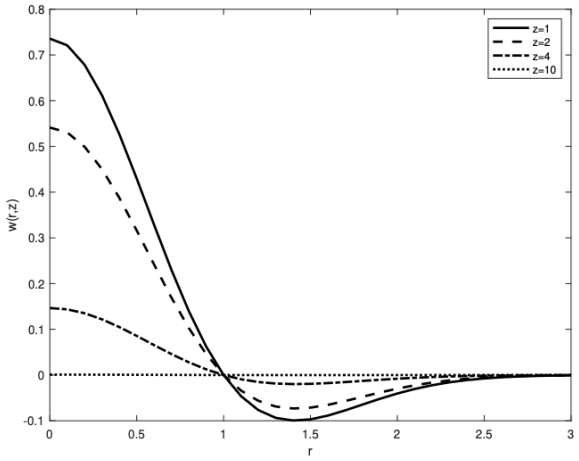

(b)

Figure 5.2: Plots for radial profiles of vertical velocity for different heights.

We observe that the maximum velocity is attained at the axis of symmetry. The maximum velocity around the axis initially increases with height until $z = 1$ is arrived at (Fig. 5.2b). However, the most interesting observation is that the wind dives a bit down around the vortex tube before it begins to rise therein and finally scales the maximum height at the axis. This is reflected through negative vertical velocity outside around the vortex periphery, which is uniformly zero beyond it. A further observation is that the wind scales greater heights when it dives down more towards the ground.

5.3.3 Azimuthal velocity $v(r, z)$

The Azimuthal velocity is the most significant component of velocity in vortex motion. Its dependence exclusively on the radial coordinate in the majority of the earlier theoretical models is a crude estimation of the real phenomenon, as the axial coordinate also plays a significant role in the growth of the vortex. For this reason, in this article, the azimuthal component of velocity is obtained to depend on radial and vertical directions. We plot graphs to analyse the radial dependence of azimuthal velocity. Figs. (5.3) display the variation of the azimuthal component. Fig. (5.3a) is based on Eqs. (5.19, 5.21) while Fig. (5.3b) on Eq. (5.26). The obtained azimuthal component expression includes an undetermined function $A(r)$ as a part of an integration performed for z, which we determine using two different classical vortex models, viz., Rankine and Burgers. We, therefore, discuss two cases in which we use the Rankine velocity as the initial condition at $z = 0$ in the former and Burgers velocity in the latter case.

Case 1. We study the radial variation of the azimuthal velocity with the Rankine velocity as the initial condition (Fig. 5.3a). The azimuthal velocity is observed to increase to the maximum in the core region and further decrease to zero. We compare the azimuthal velocity profile of this model, which has (r,z)-dependent velocity, with that of the Rankine

model, which is independent of z. In the Rankine model, the radial profile of the azimuthal velocity in the core region is linear and falls off in the outer region, whereas in this model, it is slightly curved in the core region but similar in the outer region. The difference in the radial profiles in the two models is an indication that the wind rotation inside the core is a little slower than what Rankine predicted. Another observation is that the rotational velocity slightly increases with height. Besides, the azimuthal component takes a sharp turn at the core, falls from the peak, and seems to weaken asymptotically.

Case 2. Fig. (5.3b) represents the radial distribution of the azimuthal velocity with the Burgers model as the boundary condition. This graph is plotted for the range $z = 0.1 - 0.8$. The azimuthal velocity increases in the core region. Unlike the aforementioned case, the velocity profile remains smooth even when it crosses the core and steps into the outside region. The fact worth noticing is that the core radius is not necessarily the region of the maximum wind; it rather appears before the wind reaches the core, and by the time it arrives at the core, the rotational velocity declines drastically. It may be noted that by assigning a suitable value to a particular parameter present in the Burgers model, researchers succeeded in bringing the peaks of the rotational velocity curves of the Burgers and the Rankine models at the same radial distance for the sake of comparison.

The impact of the Reynolds number on the azimuthal velocity is also examined for the two cases. The Reynolds number for atmospheric vortices lies in the range of $1000 - 10000$. However, for the sake of plot clarity and for subsequently drawing inference, the Reynolds number varies in the range of $10 - 1000$. The plots are shown in Figs. (5.3c-d). Fig. (5.3c), meant for Case 1, reveals that in the close vicinity of the core radius, the azimuthal velocity for lower Reynolds numbers slightly exceeds that for higher Reynolds numbers. Farther from the core, the azimuthal component curves merge irrespective of the Reynolds number, divulging the ineffectiveness of viscosity.

Near the core region of Case 2, the wind rotation for lower Reynolds numbers exceeds that for higher Reynolds numbers and is reversed in the core's immediate outskirts, but beyond that, the Reynolds number fails to affect the rotational velocity. Thus, the viscosity effect is similar to that of Case 1 but the magnitude is many folds higher. This leads to the conclusion that the viscosity of the fluid plays a big role to determine the pattern of the velocity in the immediate neighbourhood of the core region. However, in regions farther from the core radius, the viscosity effects are insignificant.

Refan et al. (2017) gave a velocity profile analysis using the ground-based velocity track display method on Doppler radar data on tornadoes. They simulated the collected data for different heights against Rankine and modified Rankine models. Although the agreements were claimed, but this is worth noting that in neither of the models height of the vortex is a parameter. However, the radial profiles of azimuthal velocity given by Refan et al. (2017) are in good agreement with those of this model. One can observe that the azimuthal velocities, obtained in Case 1 and Case 2 both, have a good resemblance with the various plots of the azimuthal velocity analysed by Refan et al. (2017). Particularly profiles in Case 2 are everywhere differentiable match more closely with the experimental data. Similar profiles of azimuthal velocity can be seen in some of the laboratory researchers on tornado-like vortices (Refan et al. (2014), Horn and Aurnou (2021)).

It is further observed that contrary to the trends of the rotational velocity, shown by the corresponding curves, in Figs. (5.3), the velocity is enormously dependent on height (Figs. (5.3)-(5.4)). At lower altitudes, the azimuthal component rises closer to the axis, diminishes in its outer neighbourhood and then once again tends to rise. The magnitude of the latter rise of the azimuthal velocity gradually declines with height. At considerably high altitudes, the latter rise becomes insignificant. Such variations were never observed in Figs. 5.3(a, c). The variations in the rotational velocity are in the vicinity of the core but not within the core region. The core is identifiable in the velocity curves by the points at

which the second time curvature changes direction (Figs. 5.3b, 5.4c). In particular cases, the core radius may be the radius of the maximum wind (Figs. 5.4a-c).

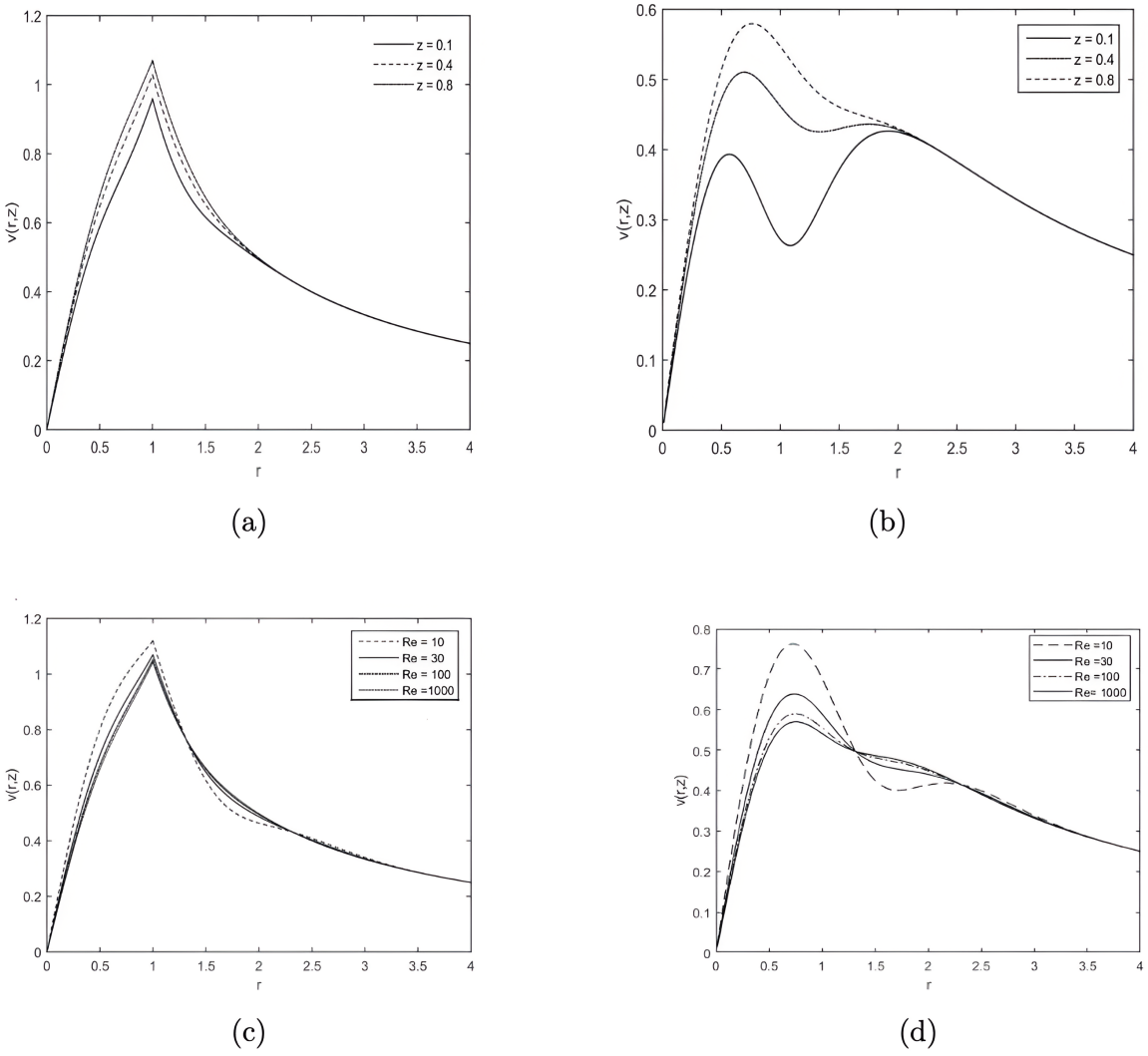

Figure 5.3: Plots (3a), (3b) represent the radial variation of Azimuthal velocity $v(r, z)$ for height $z = 0.1 - 0.8$ based on respectively the Rankine model and the Burgers model while plots (3c), (3d) correspond to respectively the radial variation of azimuthal velocity with Reynolds number based on Rankine and Burgers models. The other parameters are $\alpha = 1$ and $k = 0.5$.

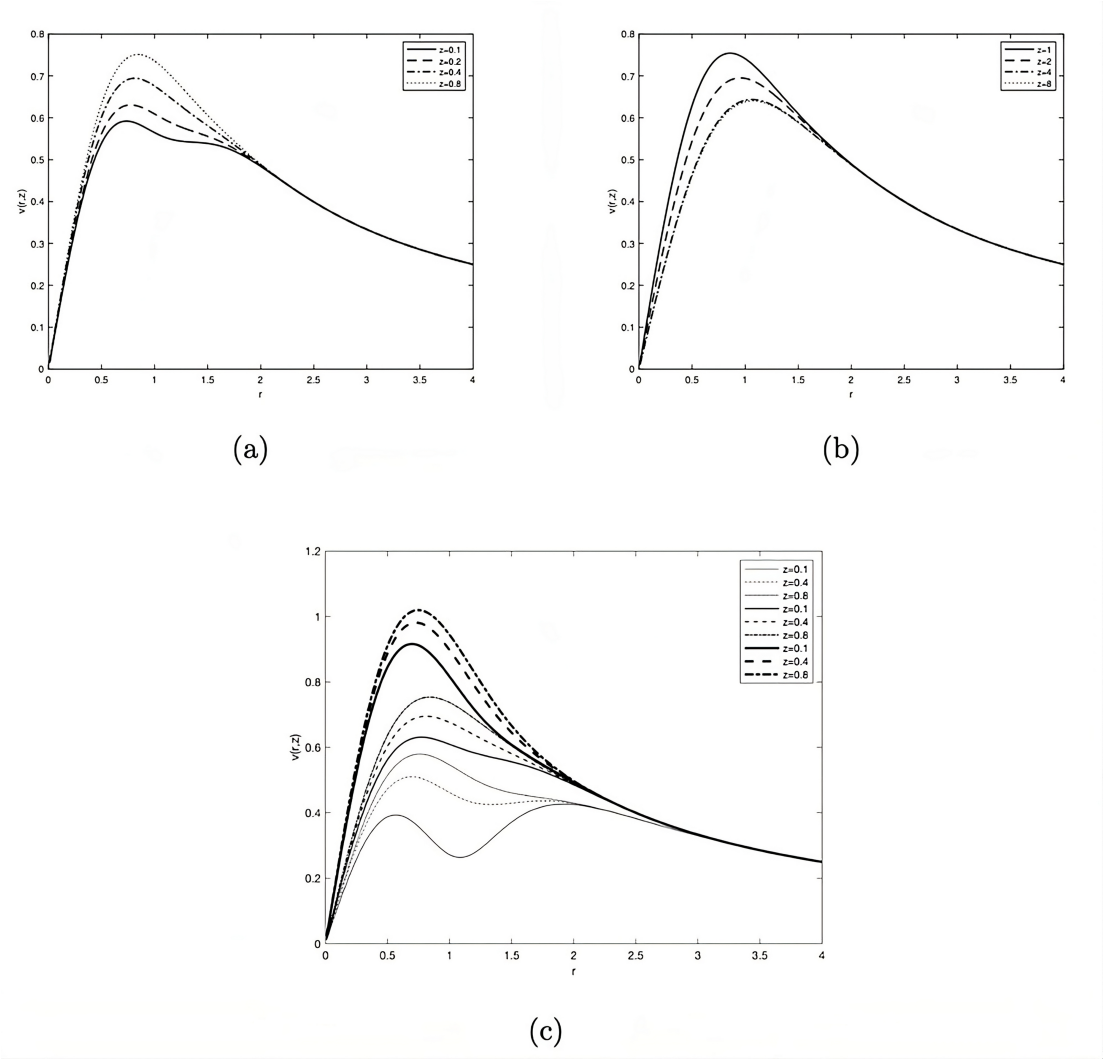

Figure 5.4: Plots (a-b) represent the radial variation of azimuthal velocity $v(r, z)$ for heights $z = 0.1 - 1$ and $z = 1 - 10$ for $\alpha = 1$ and $K = 1$ based on the Burgers model respectively while Fig.(4c) displays the radial profiles of azimuthal velocity for different heights corresponding to $K = 0.5, 1, 2$.

It is also observed that, unlike Rankine's pointed curves, Burgers' smooth curves reveal that at lower altitudes, the azimuthal velocity falls immediately after it reaches its peak (Fig. 5.3b). It may be noted that $\alpha = 1$ and $k = 0.5$ for Fig. (5.3d). However, it once again rises and joins other curves drawn for higher altitudes beyond a certain radial distance. This fall of azimuthal velocity just after its peak diminishes in magnitude as one goes vertically upwards. Further, such falls are observed for low Reynolds numbers (Fig.

5.3d) or with decreasing k , here for $k = 0.5$ (Fig. 5.4c). Comparing Fig. (5.3b) and Fig. (5.4c), we find that $k = 0.5$ which may be responsible for the falls under discussion. However, the values assigned to k are arbitrary. Moreover, falls in azimuthal velocity are observed for very low Reynolds numbers, hence due to high viscosity.

In order to investigate the impacts of α and k, we need to consider Figs. (5.3b, c) together with Figs. (5.4). Figs.(5.4a,b) are plotted for $\alpha = 1$, $k = 1$ and the height ranges in $z = 0 - 1$ (Fig. 5.4a) and $z = 1 - 10$ (Fig. 5.4b). It is found that the azimuthal velocity increases with height in the range $z = 0 - 1$, while, contrary to this, the azimuthal component diminishes with height above $z = 1$. A remarkable point is that the maximal azimuthal velocity represented by the peak value of all curves moves away from the axis with height irrespective of whether the azimuthal velocity increases or decreases with height. It gives a funnel shape to the whirlwind.

Fig. (5.4c) reveals the impact of k. It is varied in the range $k = 0.5 - 2$ with $\alpha = 1$. It is observed that the azimuthal velocity which increases with height further increases with k, the maximum distinction being around the core. However, all the curves merge beyond certain radial distance from the axis revealing the fact that ultimately height and k do not affect the azimuthal velocity.

The velocity curves for the azimuthal component plotted in Fig. (5.5) correspond to three distinct sets $\alpha = 0.5, 1, 1.5$. Each set comprises azimuthal velocities at three distinct heights $z = 0.3, 0.6, 0.9$. Solid curves, as elaborated in the caption, correspond to $z = 0.3$, dashed curves to $z = 0.6$ and centre curves to $z = 0.9$. It is observed that azimuthal velocity increases with α and z as well, as already discussed in Figs. (5.3, 5.4). The set of curves corresponding to $\alpha = 0.5$ are maximally inclined whereas that corresponding to $\alpha = 0.5$ is least inclined to the r-axis; the velocity curves corresponding to $\alpha = 1$ are lying in between the other two sets.

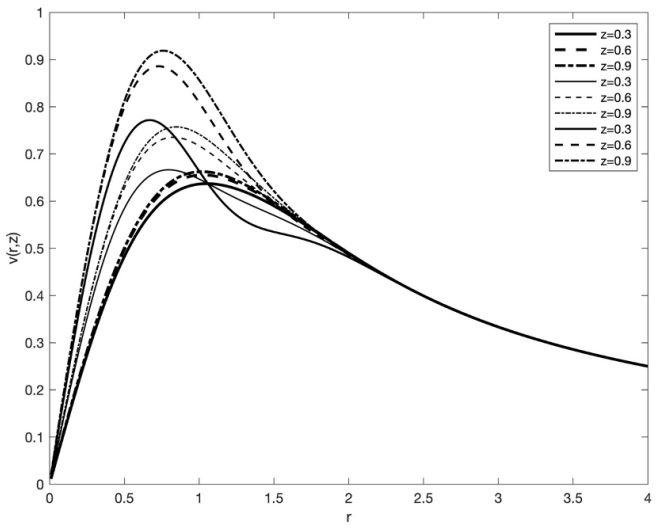

Figure 5.5: The curves in the plot corresponds to three distinct sets ($\alpha = 0.5, 1, 1.5$) of azimuthal velocities drawn at three distinct heights $z = 0.3, 0.6, 0.9$. Solid curves correspond to $z = 0.3$, dashed curves to $z = 0.6$ and centre curves to z=0.9. The set of curves corresponding to $\alpha = 0.5$ has minimum gradient to t3he r-axis, that corresponding to $\alpha = 1$ has the next greater gradient while that corresponding to $\alpha = 1.5$ is least inclined to the r-axis.

It is observed in Fig. (5.5) that the azimuthal velocity which depends on height is more distinguishable when α increases. Although not drawn in the plot, velocity curves corresponding to different heights for still lower values of α are virtually indistinguishable.

$\alpha \leq 1$ means that $r_m \leq L$ while $\alpha \geq 1$ means that $r_m > L$. They respectively relate to dust devils and hurricanes. Hence it is concluded that the azimuthal velocity remains almost the same along the entire length in dust devils while, in contrast, it varies continuously along the length in hurricanes. However, a reverse trend above $z = 1$ is speculated (Fig. 5.4b).

This model presents a comprehensive analysis of atmospheric vortices. In Case 1, we illustrate the azimuthal velocity pattern characterizing small-scale vortices. In this case, the rotational velocity is prominent within the core region but gradually diminishes beyond. Conversely, Case 2 shows the rotational profile observed in large-scale vortices.

In these instances, the velocity exhibits a core with increasing intensity, followed by a gradual decline as one moves away from the centre. This study reveals a common thread in both scenarios, where there is a smooth increase in velocity within the core, followed by a fluctuation in the velocity, which is particularly evident in the region of the rain-band (region of updrafts and downdrafts). Beyond the rain band, the velocity dissipates.

5.3.4 Radial Pressure

A main factor for the development of vortex motion is the radial pressure distribution. Due to a substantial pressure difference between the axis and the outer boundary, atmospheric vortices occur in nature. The axial pressure gradient is deduced by substituting the assumed radial velocity and derived axial velocity from the continuity equation into the z-momentum Eq. (5.8). Integration of the resulting equation gives pressure. To evaluate the undetermined function of integration $A(r)$, we use two different models as a boundary condition at $z = 0$. We assume the flow to be in the Cyclostrophic balance i.e. $v^2/r = \partial p/\partial r$. First, we use the Rankine model as a boundary condition, pressure distribution is given by Eqs. (5.20, 5.22). Figs. 5.5(b, d) depict the change in the radial pressure difference obtained by means of Rankine and Burgers models respectively. We describe the dependence of Reynolds number on radial pressure distribution based on the Rankine and the Burgers boundary conditions respectively in Figs.5.6(a, c).

In Fig (5.6a), we observe that for $Re = 10$, pressure increases along radius, except within a small region near the axis, however. The pressure grows exponentially with radius without any exceptions for higher Reynolds numbers. We conclude that as the Reynolds number increases, so does the pressure with radius. Here too $k = 0.5$, we have already observed a sudden fall in azimuthal velocity when either $k = 0.5$ (Figs. 5.3b, 5.4c) or $Re = 10$ (Fig. 5.3d). A similar depression in pressure may be due to the same reasons.

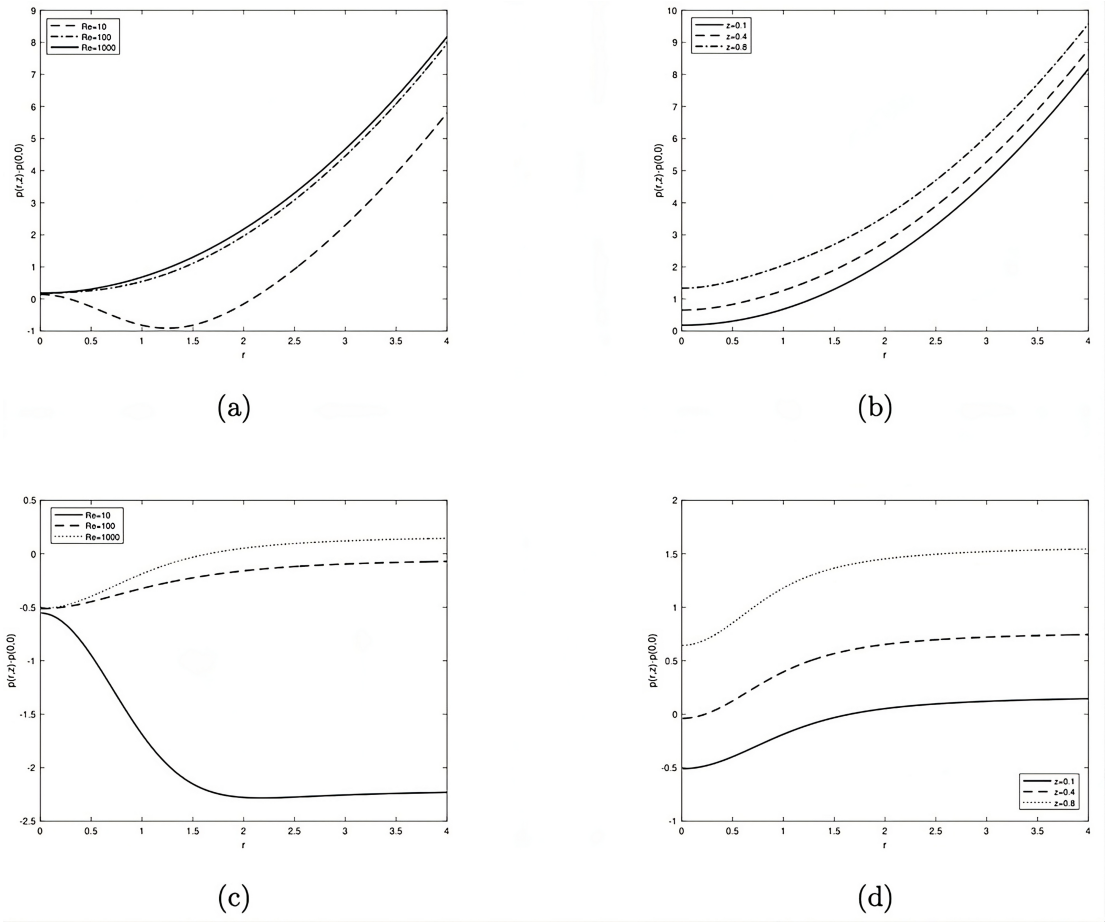

Figure 5.6: Plot for (a) and (c) represents Pressure difference $p(r,z) - p(0,0)$ vs. radius r for Reynolds number $Re = 10, 100$ and 1000 based on Rankine and Burgers model respectively, (b) and (d) represents pressure difference $p(r,z) - p(0,0)$ with respect to radius r at different values of vertical height $z = 0.1 - 0.8$ based on the Rankine model and Burgers model respectively.

We further analyse the dependence of the radial pressure for high Reynolds numbers. The radial pressure increases from the axis towards the core and its outer region. The radial pressure is also observed to increase with height z of the atmospheric vortex.

In Fig. (5.6c), which corresponds to the Burgers model, we observe that for the Reynolds number $Re = 10$, the radial pressure falls from the axis almost to the core and continues to be almost the same. Unlike this, for higher Reynolds numbers it rises in the same range and continues to be the same beyond that.

In Fig. (5.6a), we observe that for $Re = 10$, pressure increases along radius, except within a small region near the axis, however. The pressure grows exponentially with radius without any exceptions for higher Reynolds numbers. We conclude that as the Reynolds number increases, so does the pressure with radius. Here too $k = 0.5$, we have already observed a sudden fall in azimuthal velocity when either $k = 0.5$ (Figs.5.3b, 5.4c) or $Re = 10$ (Fig. 5.3d). A similar depression in pressure may be due to the same reasons.

We further analyse the dependence of the radial pressure for high Reynolds numbers. The radial pressure increases from the axis towards the core and its outer region. The radial pressure is also observed to increase with height z of the atmospheric vortex.

In Fig. (5.6c), which corresponds to the Burgers model, we observe that for the Reynolds number $Re = 10$, the radial pressure falls from the axis almost to the core and continues to be almost the same. Unlike this, for atmospheric vortices for which Reynolds numbers are high, it rises in the same range and continues to be the same beyond that.

Once again, for higher Reynolds numbers, we further analyse the impact of height. Fig. (5.4d) exhibits that the radial pressure, corresponding to the Burgers model, increases within the core but remains the same outside. This is worth noting that, in contrast with the Rankine case; the changes do not take place sharp at the core but smoothly in its neighbourhood.

5.4 Conclusion

Radial velocity was assumed a function of radial and axial coordinates both, as suggested by Onishchenko et al. (2021b), which yields a generalised model for atmospheric vortices with other velocity components also depending on the said coordinates. Unlike similar models, this considers the axi-symmetric flow of a viscous fluid. For derivation of those

components of velocities, the Rankine (1882) and the Burgers (1948) models were used as the boundary condition for imposing cyclostrophic balance. All of the velocity components of this model are bounded.

This model incorporates exponential localization not only in the radial direction but also in height, yielding a novel vortex structure with distinct regions in the radial direction: an inner region facilitating upward flow and an outer region directing flow downward. Notably, the present model distinguishes itself from previous approaches by providing a comprehensive characterization of vortex parameters. We consider not only the characteristic vortex radius, denoted as r_m, but also introduce a vortex height, labelled as L. Moreover, this model is designed for viscous flow, a significant improvement over the inviscid flow of the Onishchenko et al. model. The key innovation in our approach lies in the bounded nature of all three non-zero velocities in both the radial and axial directions, setting it apart from the previous models. This enhances the applicability of the present model in describing vortex phenomena.

Considering the wind blowing towards the axis of symmetry, it is observed that the radial velocity, which is height-dependent in this model, increases in magnitude to the maximum at the outer boundary of the core, and decreases as it enters the core region to ultimately vanish at the axis. Moreover, the radial velocity reduces in magnitude with height.

The vertical velocity is maximum at the axis but gradually decreases off the axis along the radius to eventually vanish. The maximum velocity around the axis initially increases with height. However a reverse trend is observed once it reaches the characteristic height. A further observation is that the wind scales greater heights when it dives down more towards the ground.

It is inferred that in addition to viscous effects and the impact of the altitude consideration, the patterns of the velocity components are very much dependent on the models used as boundary conditions. The azimuthal velocity derived with the Rankine model as the boundary condition shows a sharp turn at the core layer where it is maximum and increases with height but not linearly as seen in the classical Rankine model, while the changes are smooth near the core and not necessarily maximum at the core when the boundary condition imposed is the Burgers model. Further at lower altitudes, the azimuthal component rises with variations. It declines with height. The core radius is not necessarily the radius of the maximum wind for the latter case. The azimuthal velocity initially increases with height but once it reaches the characteristic height, it starts diminishing. A point to be noted is that the maximal azimuthal velocity represented by the peak value of all curves moves away from the axis with height irrespective of whether the azimuthal velocity increases or decreases with height. It gives a funnel shape to the whirlwind.

The azimuthal velocity which increases with height further gets augmented with k, the maximum distinction being around the core. However, it is the same beyond certain radial distance from the axis revealing that height and k siege to impact the azimuthal velocity. It is more distinct when the radius of maximum wind increases. It is concluded that the azimuthal velocity remains almost the same along the entire length in small-scale vortices but varies continuously along the length in large-scale vortices. A reverse trend is speculated above the characteristic height.

The impact of viscosity is enormous in the immediate neighbourhood of the core radius. The azimuthal velocity shows a reverse trend in the inner and the outer regions close to the core radius. However, viscosity fails to influence the velocity profile far distant from the core radius.

The radial pressure is more in the outer region and lessens gradually in the core to vanish at the axis in both cases. But the pressure distributions outside the core are distinct in the sense that in the first case, it seems to diminish while in the second it remains the same. The radial pressure is also observed to increase with height. For low Reynolds numbers, i.e., for higher viscosity, at lower altitudes, the radial pressure is observed to increase within the core towards the axis. This is a deviation from the practical experience or just an anomaly at lower heights. This may also be due to some weak considerations in modelling.

Appendices

Appendix A

In this subsection, we determine $A(r)$ in the inner region $r = \tilde{r}/r_m \leq 1$ of the vortex. Initially, we assume that the flow is in the cyclostrophic balance at $z = 0$, i.e.

$$\frac{\partial p(r,0)}{\partial r} = \frac{v^2(r,0)}{r}. \tag{5.A.1}$$

We further assume that at $z = 0$, the flow is a solid body rotation. Substituting $v(r,0) = r$ for $r = \tilde{r}/r_m \leq 1$, into (A) we get $\partial p(r,0)/\partial r = r$, which, on substituting into Eq.(18), yields

$$A(r) = -\alpha\frac{r^2}{2} - \frac{2}{Re}\Big(4(-2+4r^2-r^4) + \alpha^2(r^2-1)\Big)e^{-r^2} + C_1. \tag{5.A.2}$$

where constant C has been replaced by C_1 for this case, for the sake of clarity. Substituting Eq. (5.17) along with Eq. (5.A.1) into Eq.(5.16), we get the azimuthal velocity as

$$v(r,z) = \Bigg[r^2\{\alpha^2(1-2r^2+z(2-z))+8z^2\}e^{-2(z+r^2)} - \frac{1}{Re}\Bigg(8\alpha(2-r^2)(1-z) - \alpha^3(3-z) + \frac{16}{\alpha}(6-6r^2+r^4)(1+z)\Bigg)e^{-(z+r^2)} + \frac{r}{\alpha}\Bigg(\alpha r + \frac{4r}{Re}\{2(6-6r^2+r^4) - \alpha(2-r^2)\}e^{-r^2}\Bigg)\Bigg]^{1/2}. \tag{5.A.3}$$

Substituting Eq. (5.A.2) into Eq. (5.14), we get pressure as

$$-\alpha p + zF = 2\alpha z^2 e^{-2(z+r^2)} - \frac{2}{Re}\Bigg(4(1+z)(2-4r^2+r^4) + \alpha^2\{(1-z)(1-r^2)\}\Bigg)e^{-(z+r^2)} - \alpha\frac{r^2}{2} - \frac{2}{Re}[4(-2+4r^2-r^4) + \alpha^2(r^2-1)]e^{-r^2} + C_1, \tag{5.A.4}$$

Suppose $p(0,0)$ (some finite value), using this condition in Eq. (5.22), we get $C_1 = -\alpha p(0,0)$, substituting it into Eq.(5.A.4), we get

$$-\alpha\{p(r,z) - p(0,0)\} = -zF + 2\alpha z^2 e^{-2(z+r^2)} - \frac{2}{Re}\Bigg(4(1+z)(2-4r^2+r^4) + \alpha^2\{(1-z)(1-r^2)\}\Bigg)e^{-(z+r^2)} - \alpha\frac{r^2}{2} - \frac{2}{Re}\Bigg(4(-2+4r^2-r^4) + \alpha^2(r^2-1)\Bigg)e^{-r^2} \tag{5.A.5}$$

Appendix B

We determine $A(r)$ in the region $r = \tilde{r}/r_m \geq 1$ of the vortex. The flow is in the cyclostrophic balance, i.e. $\frac{\partial p(r,0)}{\partial r} = \frac{v^2(r,0)}{r}$. Now we assume that at $z = 0$, the flow has velocity $v(r,0) = \frac{1}{r}$ for $r \geq 1$. Substituting $v(r,0) = \frac{1}{r}$ for $r = \tilde{r}/r_m \geq 1$, into $\frac{\partial p(r,0)}{\partial r} = \frac{v^2(r,0)}{r}$, we get

$$\frac{\partial p(r,0)}{\partial r} = \frac{1}{r^3}. \tag{5.B.1}$$

Substituting Eq. (5.B.1) into Eq. (5.18), we obtain

$$A(r) = \frac{\alpha}{2r^2} - \frac{2}{Re}\Big(4(-2+4r^2-r^4) + \alpha^2(r^2-1)\Big)e^{-r^2} + C_2, \tag{5.B.2}$$

where integrating constant C has been replaced by C_2 for the sake of clarity. Eq. (5.16), in view of Eq. (5.17) and Eq. (5.B.1), yields the azimuthal velocity as

$$\begin{aligned} v(r,z) = \Bigg[& r^2\{\alpha^2(1-2r^2+z(2-z)) + 8z^2\}e^{-2(z+r^2)} - \frac{1}{Re}\Big(8\alpha(2-r^2)(1-z) \\ & - \alpha^3(3-z) + \frac{16}{\alpha}(6-6r^2+r^4)(1+z)\Big)e^{-(z+r^2)} + \frac{r}{\alpha}\Big(\frac{\alpha}{r^3} + \frac{4r}{Re}\{2(6-6r^2+r^4) \\ & - \alpha^2(2-r^2)\}e^{-r^2}\Big)\Bigg]^{1/2}. \end{aligned} \tag{5.B.3}$$

We obtain pressure from Eq. (5.14) by substituting for $A(r)$ from Eq.(5.B.2) as

$$\begin{aligned} -\alpha p + zF = {} & 2\alpha z^2 e^{-2(z+r^2)} - \frac{2}{Re}\Big(4(1+z)(2-4r^2+r^4) + \alpha^2\{(1 \\ & - z)(1-r^2)\}\Big)e^{-(z+r^2)} + \frac{\alpha}{2r^2} - \frac{2}{Re}\Big(4(-2+4r^2-r^4) + \alpha^2(r^2-1)\Big)e^{-r^2} + C_2, \end{aligned} \tag{5.B.4}$$

where C_2 is an integration constant to be determined by using boundary condition on $p(r=1,0)$. Substituting $r=1$, $z=0$ into Eq. (5.27), we get $C_2 = -\alpha p(1,0) - \alpha/2$, substituting into Eq. (5.27), we get

$$\begin{aligned} -\alpha\{p(r,z) - p(1,0)\} = {} & -zF + 2\alpha z^2 e^{-2(z+r^2)} \\ & - \frac{2}{Re}\Big(4(1+z)(2-4r^2+r^4) + \alpha^2\{(1-z)(1-r^2)\}\Big)e^{-(z+r^2)} \\ & + \frac{\alpha}{2}\Big(\frac{1}{r^2} - 1\Big) - \frac{2}{Re}\Big(4(-2+4r^2-r^4) + \alpha^2(r^2-1)\Big)e^{-r^2}. \end{aligned} \tag{5.B.5}$$

Appendix C

Substituting Eq. (5.24) into Eq. (5.14), we obtain

$$-\alpha p+zF = 2\alpha z^2 e^{-2(z+r^2)} - \frac{2}{Re}\Bigg(4(2-4r^2+r^4)(1+z)+\alpha^2\{(1-r^2)(1-z)\}\Bigg)e^{-(z+r^2)} - \alpha\int\frac{(1-e^{-Kr^2})^2}{r^3}dr - \frac{2}{Re}\Bigg(4(-2+4r^2-r^4)+\alpha^2(r^2-1)\Bigg)e^{-r^2}+C. \tag{5.C.1}$$

Moreover, substituting $r=0$ and $z=0$ in Eq.(5.C.1), we get

$$C = -\alpha p(0,0) + \alpha\Bigg(\int\frac{(1-e^{-Kr^2})^2}{r^3}dr\Bigg)_{r=0},$$

in view of which Eq.(5.C.1) yields pressure as

$$\begin{aligned}\{p(r,z)-p(1,0)\} = \frac{-1}{\alpha}\Bigg[&-zF+2\alpha z^2e^{-2(z+r^2)}\\ &-\frac{2}{Re}\Bigg(4(1+z)(2-4r^2+r^4)+\alpha^2\{(1-z)(1-r^2)\}\Bigg)e^{-(z+r^2)}\\ &-\alpha\Bigg[\int\frac{(1-e^{-Kr^2})^2}{r^3}dr-\Bigg(\int\frac{(1-e^{-Kr^2})^2}{r^3}dr\Bigg)_{r=0}\Bigg]\\ &-\frac{2}{Re}\Bigg(4(-2+4r^2-r^4)+\alpha^2(r^2-1)\Bigg)e^{-r^2}\Bigg].\end{aligned} \tag{5.C.2}$$

****